RESEARCH ARTICLE

Achieving the High Capacity and High Stability of Li-Rich Oxide Cathode in Garnet-Based Solid-State Battery

Butian Chen,[a] Jicheng Zhang[a], Deniz Wong[b], Tenghui Wang[a], Taiguang Li[a], Chong Liu[a], Limei Sun[c] and Xiangfeng Liu *[a]

[a] PhD student, B. Chen, Professor, J. Zhang, Master Degree Candidate, T. Wang, PhD student, T. Li, PhD student, C. Liu and Professor, X. Liu
Center of Materials Science and Optoelectronics Engineering, College of Materials Science and Optoelectronic Technology
University of Chinese Academy of Sciences
Beijing
E-mail: liuxf@ucas.ac.cn

[b] Dr. D. Wong
Helmholtz-Zentrum Berlin für Materialien und Energie
Hahn-Meitner-Platz 1, D-14109 Berlin
Germany

[c] Professor L. Sun
Department of Nuclear Physics
China Institute of Atomic Energy
Beijing

Abstract: Solid-state batteries (SSBs) based on Li-rich Mn-based oxide (LRMO) cathodes attract much attention because of their high energy density as well as high safety. But their development was seriously hindered by the interfacial instability and inferior electrochemical performance. Herein, we design a three-dimensional foam-structured GaN-Li composite anode and successfully construct a high-performance SSB based on Co-free $Li_{1.2}Ni_{0.2}Mn_{0.6}O_2$ cathode and $Li_{6.5}La_3Zr_{1.5}Ta_{0.5}O_{12}$ (LLZTO) solid electrolyte. The interfacial resistance is considerably reduced to only 1.53 Ω cm^2 and the assembled Li symmetric cell is stably cycled more than 10,000 h at 0.1-0.2 mA cm^{-2}. The full battery shows a high initial capacity of 245 mAh g^{-1} at 0.1C and does not show any capacity degradation after 200 cycles at 0.2C (~100%). The voltage decay is well suppressed and it is significantly decreased from 2.96 mV/cycle to only 0.66 mV/cycle. The SSB also shows a very high rate capability (~170mAh g^{-1} at 1C) comparable to a liquid electrolyte-based battery. Moreover, the oxygen anion redox (OAR) reversibility of LRMO in SSB is much higher than that in liquid electrolyte-based cells. This study offers a distinct strategy for constructing high-performance LRMO-based SSBs and sheds light on the development and application of high-energy density SSBs.

Introduction

High-energy-density lithium-ion batteries (LIB) can greatly improve the alleviation of mileage anxiety in electric vehicles and promote the rapid development of portable electronics and energy storage power stations. [1-3] However, traditional lithium-ion cathode materials, whether it is layered structure ($LiCoO_2$, $LiNi_xCo_yMn_{1-x-y}O_2$, $LiMnO_2$), olivine structure ($LiFePO_4$) or spinel structure ($LiMn_2O_4$), its specific capacity has reached a bottleneck and is difficult to break through (its specific capacity is lower than 200 mAh g^{-1}). [4-7] Therefore, the development of new high-energy cathode materials has become very urgent. Lithium-rich Mn-based oxide (LRMO) cathode materials have been widely investigated as the next generation of cathode materials due to their ultra-high specific capacity (>300 mAh g^{-1}) and high energy density (~1000 Wh kg^{-1}). [8] But the critical issues such as irreversible lattice oxygen loss (oxygen gas release), voltage decay and rapid capacity decay accompanying the cycling process have seriously hindered the practical application of LRMO cathode materials. [9,10]

The liquid electrolyte (LE) is known as the blood of the LIB, and its impact on battery performance cannot be overstated. However, organic solvents in LE are one of the major causes of fire and explosion in LIB, which has a huge impact on the security of LIB. [11,12] LRMO cathodes with high voltage and high specific energy characteristics, on the other hand, put forward higher requirements for LE. Lattice oxygen released from the LRMO cathode under high pressure will lead to the decomposition of the LE, and the decomposed LE will seriously corrode LRMO cathode and lead to the dissolution of transition metals (TM). [13,14] This is one of the major reasons for the poor cycling performance and fast voltage decay of the LRMO cathode. [15-17] Therefore, the use of solid electrolytes (SE) with LRMO cathode is one of the best choices to solve critical issues. But the unique oxygen anion redox (OAR) and the high operating voltage (4.8V) of LRMO cathode, and the critical issues such as oxygen release, irreversible phase transition and increased interfacial resistance seriously restrict their application in solid-state batteries (SSB). To the best of our knowledge, there are only a few reports on the evaluation of LRMO cathode materials in SSB. [18-20] Pan et al. used Li_6PS_5Cl (LPSCl) SE to evaluate the composite cathode of LRMO/$LiNiO_2$, which achieved 85% capacity retention at 0.1C for 100 cycles. [20] Zhang et al. used 20% Li_2SO_4 mixed with LRMO cathode, followed by $Li_3InCl_{4.8}F_{1.2}$ SE to evaluate the performance of the battery, and its capacity retention rate could reach 80.1% after 100 cycles at 0.2C. [19] Recently, Sun et al. assembled an SSB using LRMO cathode with a surface-deposited Li_3PO_4 layer and Li_3InCl_6 SE, and its capacity retention could be improved to 87.9% after 100 cycles at 0.2C. [18] These pioneer studies have shown the great potential of LRMO-based SSB. But the rate capability is quite low and the specific capacity at a high current density of 1C is only around 120-130 mAh g^{-1} due to the interfacial instability [19,20]. Moreover, it is well known that voltage decay is one of the most critical issues for Li-rich oxide cathodes, and it is quite important to know the voltage behavior of Li-rich oxide cathodes in SSBs. But the voltage behaviors of LRMO-based SSBs have not been reported in the previous few studies. [18-20] In addition to the voltage behaviors, the OAR characteristics of LRMO, which have a decisive role in the electrochemical performances in LE-based cells, are also far less known in LRMO-based SSBs. Therefore, how to enhance the long-term cycling stability, the rate capability and the voltage retention remains a highly challenging issue for LRMO-based SSBs.

Garnet-type SE $Li_{6.5}La_3Zr_{1.5}Ta_{0.5}O_{12}$ (LLZTO) has high Li^+ conductivity and a wide electrochemical window,[21] which can be an ideal SE used to evaluate LRMO in SSB. But the huge Li|LLZTO interfacial resistance and the Li dendrite concerns hinder the use of LLZTO in LRMO-based SSB. [22] To solve these issues, in this work, we design a three-dimensional (3D) foam-structured GaN-Li composite anode and successfully construct a high-performance SSB based on LLZTO SE and Co-free LRMO cathode (unmodified bare $Li_{1.2}Ni_{0.2}Mn_{0.6}O_2$). The interfacial resistance was considerably reduced to only 1.53 Ω cm^2. The assembled Li symmetric cell can be stably cycled for more than 10,000 h at 0.1-0.2 mA cm^{-2}. Even at an ultra-high area-specific capacity (2.5 mAh cm^{-2}), it can still be stably cycled for more than 1500h without Li dendrite growth, demonstrating extremely superior interfacial stability. As far as we know, 1500h is also the longest time that a garnet-based SE can be cycled at such a high area-specific capacity. More impressively, the SSBs show a high initial capacity of 245 mAh g^{-1} at 0.1C and does not show any capacity degradation after 200 cycles at 0.2C（~100%）. In comparison to LE-based cells (the voltage decay is about 2.96 mV/cycle) the LRMO-based SSB only shows an average voltage decay of 0.66 mV/cycle. At the same time, its discharge-specific capacity under 1C can reach 170mAh g^{-1} showing outstanding rate performance, which is also comparable to a LE-based battery. Moreover, we for the first time, comprehensively explore the OAR of LRMO in SSB using resonant inelastic X-ray scattering (RIXS) and the results indicate that the OAR of LRMO in SSB shows a much higher reversibility than that in LE-based cells. This study

reports the high-performance SSB based on Co-free LRMO cathode and LLZTO SE in terms of high capacity retention, high voltage stability and high rate capability showing a great practicability of LLZTO in LRMO-based SSB but also presents some new insights on the OAR of LRMO in SSB. This study should accelerate the development and application of LRMO-based high-energy density SSB.

Results and Discussion

As previously reported, [23] LLZTO was prepared by a high-temperature solid-phase method. The X-ray diffraction (XRD) patterns of LLZTO show a pure cubic garnet phase (PDF#45-0109) and no impurity phases are formed (Figure S1). Scanning electron microscopy (SEM) of the LLZTO cross-section shows tightly arranged grains without cavities (Figure S2). The Li^+ conductivity of the LLZTO was measured by electrochemical impedance spectroscopy (EIS) to reach 8.4×10^{-4} S cm^{-1} (Figure S3). In a glove box, the Li foil is heated to 250°C to obtain molten Li, after which GaN powders of different mass fractions are added to the molten Li and mixed well to obtain the LGN_x(x=1~10) and 3D-$FLGN_x$(x=15~30) composite.

XRD and X-ray photoelectron spectroscopy (XPS) for the analysis of the phase structure of GaN after reaction with molten Li. Diffraction peaks of Ga metal, Li_3N, Li_xGa and Li_3GaN_2 can be detected in the 3D-FLGN15 composite (Figure S4a), implying that GaN reacted with molten Li most likely to produce the above substances. To further investigate the fundamental process of GaN reaction with molten Li, density functional theory (DFT) calculations based on thermodynamic analysis are used. The results of the ternary phase diagram of the Li-Ga-N system (Figure S4b), which lists all possible reaction equations (Table S1), indicate that Li_3N, Li_3GaN_2 and Li_xGa are unstable within the 3D-FLGN15 composite. Therefore, the proposed reaction Li + GaN → Li_3N + Li_3GaN_2 + Li_xGa is consistent with the thermodynamic tendency. As shown in Figure S4c, the high-resolution XPS spectrum of Li 1s in the 3D-FLGN15 composite can be deconvoluted into four peaks at 54.8,55.2,56.0 and 55.8 eV, attributed to Li metal, Li_xGa, Li_3N, and Li_3GaN_2, respectively. [24-28] The N 1s spectrum (Figure S4g) can be deconvoluted into three peaks 397,397.7 and 398.5 eV that can be assigned to Li_3GaN_2, GaN and Li_3N, respectively. [28-30] In addition, the Ga 3d spectrum (Figure S4f) can be fitted to four peaks concentrated at 18.5, 19.1, 20 and 20.6 eV, corresponding to Ga metal, Li_xGa, GaN and Li_3GaN_2, respectively. [28,31-33] The above analysis shows that Li metal, Ga metal, Li_3N, GaN, Li_xGa and Li_3GaN_2 are co-existing in the 3D-FLGN15 composite. In addition, time-of-flight secondary-ion mass spectroscopy (TOF-SIMS) shows that GaN^-, LiN^- and $LiGaN_3^-$ signals (from GaN, Li_3N and Li_3GaN_2, respectively) are uniformly distributed inside the 3D-FLGN15 composite (Figure S4h), a result that is consistent with XPS. At high current densities, the Li at the Li|LLZTO interface is heavily stripped resulting in a large number of voids and uneven Li deposition at the interface. [23] Li_3N has a very high Li^+ conductivity close to 10^{-3} S cm^{-1} at room temperature (RT), which improves the physical contact between the garnet and the Li metal and prevents the garnet from being reduced to Li metal. [34] These properties of Li_3N greatly improve the transport of Li^+ across the Li|LLZTO interface. Even at high current densities, the high Li^+ conductivity of Li_3N allows Li to be transported from within the bulk phase to the interface, [35] thereby avoiding the formation of voids at the interface and the occurrence of Li inhomogeneous deposition, inhibiting the growth of Li dendrites. In addition, the Li_xGa alloy has a very high chemical Li diffusion coefficient (D_{Li}) of about 10^{-8} - 10^{-6} cm^2 s^{-1} at RT. [31] A high diffusion coefficient increases the Li diffusion flux at the interface, reduces the Li nucleation overpotential and induces uniform Li deposition, achieving uniform Li^+ transport and a Li dendrite-free interface.

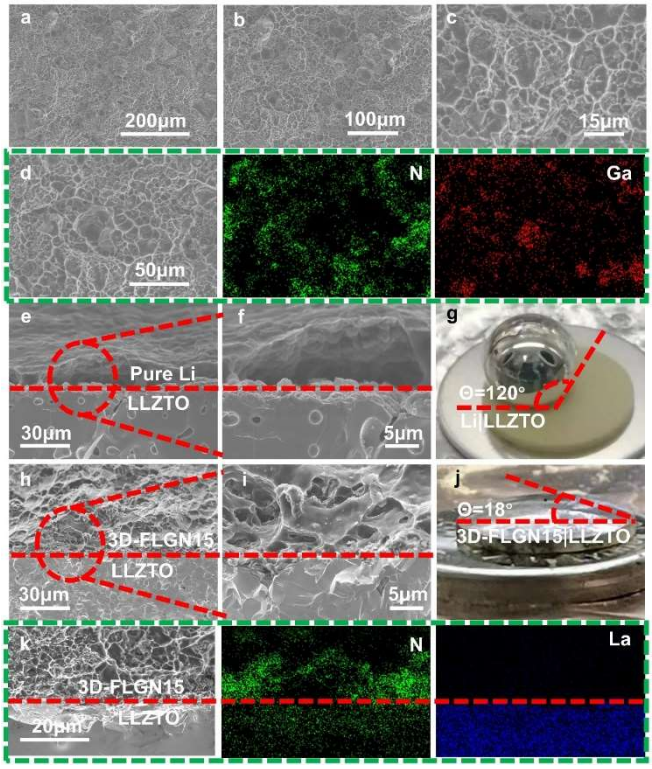

Figure 1. 3D-FLGN15 composites morphology and interfacial wettability analysis. (a-d) SEM and EDX images of cross-sections at different magnifications. (e-g) Li|LLZTO interfaces at different magnifications and CA. (h-j) 3D-FLGN15|LLZTO interfaces at different magnifications and CA. (k) EDX images of 3D-FLGN15|LLZTO interfaces.

The morphology and elemental distribution of the cross-sections of the LGN_x (x=1~30) composites were characterized by SEM coupled with an energy-dispersive X-ray detector (EDX). As shown in Figure S5, with the gradual increase of GaN content, the cross-section of LGN_x composites transforms from a flat dense structure to a 3D foam structure (Figure S5a-c), and a complete 3D macroporous foam structure is formed at a content of 15% with N and Ga elements uniformly embedded in bulk Li matrix (**Figure 1**a-d). The 3D macroporous foam structure provides a larger electroactive specific surface area and enhanced diffusion of Li^+ inside the electrode, which is essential to enhance Li^+ migration at the Li|LLZTO interface and reduce charge carrier impedance. [36] More importantly, the high specific surface area can effectively

suppress local current concentration, induce homogeneous deposition of Li^+ during the Li plating/stripping process and inhibit the growth of Li dendrites.[37] Interestingly, as the GaN content increases to 20% (Figure S5e), the cross-section maintains the 3D foam structure as it is contained, but the size of the 3D foam structure decreases dramatically and the 3D foam structure begins to collapse as the GaN content increases to 30%(Figure S5f). The contact angle (CA) is one of the most important indicators of the wettability of a Li anode to an SE and for this purpose the contact angle between pure Li|LLZTO and LGN*x* (*x*=1~30)|LLZTO was tested. As shown in Figure 1e-g, there is a huge void at the Li|LLZTO and the CA reaches 120°. In sharp contrast, the CA of LGN_x (*x*=1~30)|LLZTO is very small (Figure S6). Surprisingly, the CA of 3D-FLGN15|LLZTO is only 18° and the interfacial contact is tight (Figure 1h-j), and the same result is also verified in the EDS mapping (Figure 1k). In addition, the results of DFT calculations show that both Li metal and Li_3GaN_2 can essentially wet LLZTO (Figure S7a, S7f). It is of interest that Ga|LLZTO, GaN|LLZTO, LiGa|LLZTO and Li_3N|LLZO have more negative interfacial formation energies (-1.97 J m^{-2}, -1.94 J m^{-2}, -2.16 J m^{-2} and -2.46 J m^{-2} respectively), suggesting that GaN powder and the resulting products Ga, LiGa alloy and Li_3N from the reaction between GaN and molten Li can all improve the chemical contact between Li and LLZTO (Figure S7 b-e and g).

The area-specific resistance (ASR) of Li symmetric half-cells with LGN_x(*x*=1~30) anodes was tested using electrochemical impedance spectroscopy (EIS). As shown in Figure S8b, the Li|LLZTO|Li symmetric half-cell composed of pure Li has a very high interfacial resistance due to the generation of lithiophobic Li_2CO_3 on the LLZTO surface, the results are consistent with those reported in the literature. [38,39] In striking contrast, the addition of different proportions of GaN to the molten Li results in a significant reduction in ASR (Figure S8b). The reduction in interfacial resistance is due to the very good wetting of the LLZTO by the LGN_x(*x*=1~30) composite anode, which allows close contact between LGN_x(*x*=1~30) and LLZTO and greatly eliminates the current contraction effect caused by interfacial voids. [23] Notably, the ASR of 3D-FLGN15|LLZTO|3D-FLGN15 was only 1.53 Ω cm^2 (Figure S8c, the equivalent circuit is shown in Figure S8a) and also compared favorably with other ASRs reported in the literature (Figure S8d and Table S2). In addition, 3D-FLGN15|LLZTO|3D-FLGN15 has very low activation energy (Ea), suggesting that the unique 3D macroporous foam structure contributes to the improved transport kinetics of Li^+ at the interface (Figure S8e). A Li symmetric half-cell was used to evaluate the critical current density (CCD) and a step-increase in constant current method (fixed 0.5h Li plating and 0.5h stripping) was used to test the CCD. Due to the huge interfacial impedance, Li|LLZTO|Li short-circuits at a current density of 0.1 mA cm^{-2} (Figure S9). In contrast, the CCDs of LGN_x(*x*=1~30) anodes are all substantially higher (Figure S8f-k) and 3D-FLGN15 can reach 1.4 mA cm^{-2} (Figure S8l). The 3D-FLGN15|LLZTO|3D-FLGN15 symmetrical half-cell has a high CCD due to several factors. Firstly, Li_3N and LiGa alloys are uniformly dispersed in the 3D-FLGN15 composite anode. The high Li^+ conductivity of Li_3N inhibits the reduction of garnet to Li metal and improves the transport of Li^+ at the 3D-FLGN15|LLZTO interface, thus avoiding the occurrence of uneven Li deposition at the interface. Secondly, there is also a LiGa alloy layer with a high diffusion coefficient inside the 3D-FLGN15 composite anode, which greatly increases the diffusion flux of Li^+ at the interface and improves its energy to inhibit Li dendrites. Thirdly, the 3D-FLGN15 composite anode has very good wettability for LLZTO, which greatly reduces the resistance to Li^+ transport at the interface. Remarkably, the CCD of LGN_x(*x*=1~10) anodes with dense structure is almost always lower than that of 3D-$FLGN_x$(*x*=15~30) anodes with 3D foam structure, and 3D-FLGN15 anodes with 3D macroporous foam structure have the largest CCD, indicating that 3D foam structure anodes can improve the CCD of Li-symmetric half-cells. The 3D foam structure of 3D-FLGN15 facilitates uniform electric field distribution, reduces local currents and directs the uniform deposition of Li^+ to achieve the goal of inhibiting Li dendrite growth. [40,41]

To further understand the evolution of the interface resistance over time during cycling continuous unidirectional galvanostatic electrochemical impedance spectroscopy (GEIS) of Li symmetrical half-cells was carried out at 0.2 mA cm^{-2} current density (Figure S10a-c). Due to the very poor wettability of pure Li with LLZTO, the Li|LLZTO|Li symmetric half-cell has an interfacial resistance as high as 13959.33 Ω cm^2 just before cycling, which increases with Li stripping and terminates the cycle after 2h of Li stripping due to an overpotential exceeding the maximum voltage set by the test (Figure S10a and Figure S11). Under the same conditions, both LGN1|LLZTO|LGN1 and 3D-FLGN15|LLZTO|3D-FLGN15 symmetric half-cells showed a significant improvement in Li stripping performance. The interfacial resistance of the LGN1|LLZTO|LGN1 symmetric half-cell is below 30 Ω cm^2 for the first 7h of the cycle and suddenly increases to 572.31 Ω cm^2 at 8h (Figure S10d). The polarization voltage profiles show a sharp increase in polarization voltage due to a sharp increase in interfacial resistance and consequent termination of the test (Figure S12). Interestingly, the depth of discharge that the 3D-FLGN15|LLZTO|3D-FLGN15 symmetric half-cell can accommodate is further increased as the composite anode structure becomes a 3D foam structure. The 3D-FLGN15|LLZTO|3D-FLGN15 symmetrical half-cell can be stably Li stripping for more than 15h with an interface resistance below 20 Ω cm^2 and a very low polarization voltage (Figure S10d and Figure S13), demonstrating superior interfacial stability and the ability to accommodate deeper depths of discharge.

The distribution of relaxation time (DRT) technique is commonly used for profound analysis of EIS profiles, therefore, the DRT technique is used in this work for further analysis of GEIS results. The DRT schematic (Figure S14) shows that the whole EIS spectra will be converted as a relaxation-based function γ(τ). The peaks corresponding to the relaxation times represent the relevant electrochemical processes and the peak areas are consistent with the impedance values. [41] Where the peak appearing at $\tau < 1.6\times10^{-7}$ s comes from the impedance of the grains boundary (R_{gb}) of LLZTO. [42] The response of the anode charge transfer process then appears in the range 1.6×10^{-3}~1.6×10^{-2} s. [43] Of interest is that the response of the interfacial

Li^+ transport process appears in the range of 10^{-1}~10 s. [44] As shown in Figure S10e, all DRT peaks for the LGN1|LLZTO|LGN1 symmetric half-cell increase progressively with the Li stripping process and fail when the Li stripping capacity exceeds 1.4 mA·hour cm^{-2}. In contrast, the 3D-FLGN15|LLZTO|3D-FLGN15 symmetrical half-cell can have a Li stripping capacity of 3.0 mA·hour cm^{-2} (Figure S10f). It means that the 3D foam structure of the composite Li anode maintains interfacial contact and avoids contact loss due to the accumulation of voids. From the base equation R=ρL/S (where ρ is resistivity, L is length, and S is area), a reduction in the active area of the anode during Li stripping will result in a proportional increase in the total impedance. Due to the very large specific surface area of the 3D foam structure of the 3D-FLGN15 composite anode and the closer contact with the LLZTO (with a smaller contact angle), it has a larger active area at the interface. This significantly reduces the interfacial contact loss between 3D-FLGN15|LLZTO, improves the Li^+ transport path at the interface and improves interfacial stability.

The Li^+ diffusion coefficient (D_{Li+}) obtained by fitting the low-frequency region of the Nyquist plots is often used as a measure of the electrochemical kinetics of Li^+ transport at the interface. [45] As shown in Figure S10g, the D-value of the LGN1 composite anode is three orders of magnitude higher than that of pure Li due to the fast ionic conductivity of the LiF, Li-Ga alloy and Li_3GaN_2 components effectively improving the electrochemical kinetics of ion transport at the interface. Interestingly, the D-value of 3D-FLGN15 with its 3D foam structure is two orders of magnitude higher than that of LGN1. This is mainly because 3D-FLGN15 with a 3D foam structure has more active sites, which greatly enhances the electrochemical kinetics of the rapid diffusion of Li^+ at the interface. To further investigate the electrochemical processes at the interface, Tafel plots were fitted in the high overpotential region to obtain the exchange current density (j) of the symmetric half-cell at the interface. The 3D-FLGN15|LLZTO|3D-FLGN15 symmetric half-cell has an exchange current density of 7.869 mA cm^{-2} (Figure S10h), which is much higher than Li|LLZTO|Li and LGN1|LLZTO|LGN1 (4.051×10^{-4} and 0.37 mA cm^{-2} respectively), implying that the 3D-FLGN15|LLZTO interface is a faster ion transfer kinetic.

The long-term Li plating/stripping reversibility was analyzed using asymmetric Li-Al cells. As shown in Figure S15, with a fixed deposition capacity of 0.2 mAh cm^{-2} and a constant current density of 0.2 mA cm^{-2}, the Li|LLZTO|Al cell has a rapidly decaying and fluctuating voltage during the first cycle, when the electrode interface fails. However, LGN1 as an anode has led to a significant improvement in Li plating/stripping reversibility and can be stably cycled over 280 times with an average Coulomb efficiency (CE) of 95.0% (Figure S10i). At the same time, the LGN1|LLZTO|Al cell failed due to a sudden drop and fluctuation in voltage during the 281th cycle (Figure S16), which was due to an internal short circuit formed during the uncontrolled growth of the Li dendrites. [46] Surprisingly, 3D-FLGN15|LLZTO|Al cells can achieve an average CE of 97.2% in the first 280 cycles and maintain an average CE of 96.6% even after 450 cycles (Figure S10i-j). This result indicates that the 3D foam structure greatly improves the reversibility of the Li plating/stripping. In addition, the 3D-FLGN15|LLZTO|Al cell shows a smaller hysteresis voltage (145mV) compared to the hysteresis voltage of the LGN1|LLZTO|Al cell (e.g., 263mV in the 50th cycle, Figure S10m). After a long cycle (e.g 250 cycles), the hysteresis voltage of the 3D-FLGN15|LLZTO|Al increases by just 8mV (to 153mV, Figure S10n), while the hysteresis voltage of the LGN1|LLZTO|Al cell increases by 13.5 times (its increased hysteresis voltage is 108mV and 371mV respectively) more than that of the 3D-FLGN15|LLZTO|Al cell. The difference is that the 3D-FLGN15|LLZTO|Al cell maintains a very small hysteresis voltage even after 450 cycles (after 450 cycles the hysteresis voltage is only 176mV, Figure S10l). The very small hysteresis voltage of the 3D-FLGN15|LLZTO|Al cell is consistent with the high CE results, suggesting that the unique 3D foam structure of the composite anode can significantly improve interfacial stability and inhibit the growth of Li dendrites. Thanks to the very high Li^+ flux of the 3D foam structure, the 3D-FLGN15|LLZTO|Al cell can still be stable for more than 100 cycles (average CE of 97.3%, Figure S10o), even with higher deposition capacity and constant current density (0.5 mA cm^{-2} and 0.5 mAh cm^{-2}, respectively). And the hysteresis voltage only shows a very small fluctuation (the hysteresis voltage at the 10th and 100th times is 198mV and 214mV, respectively, Figure S10p), indicating that the 3D-FLGN15|LLZTO|Al cell still has a very high reversibility of Li release at different current densities. These results further confirm that interfacial stability and kinetics of Li plating can be greatly improved by using a composite Li anode with a 3D foam structure, enhancing the flux of Li^+ at the interface and inhibiting the growth of Li dendrites.

To further test the interface performance of 3D-FLGN15, it was subjected to a long-time galvanostatic cycling test. 3D-FLGN15|LLZTO|3D-FLGN15 symmetrical half-cell has a very small polarization (Polarization voltages of 15.2 mV and 27.5 mV at 0.1 mA cm^{-2} and 0.2 mA cm^{-2} current densities respectively) at current densities of 0.1-0.2 mA cm^{-2} and can be cycled stably for more than 10,000h during long cycle tests (**Figure 2**a). To verify whether the 3D-FLGN15|LLZTO|3D-FLGN15 symmetrical half-cell is short-circuited during a long-time of galvanostatic cycling, the impedance values for 0.1 mA cm^{-2} and 0.2 mA cm^{-2} current densities were calculated by Ohm's law to be 152 Ω cm^2 and 137.5 Ω cm^2 respectively, which are very close to the values obtained in the actual test (Figure S8b), indicating that the 3D-FLGN15|LLZTO|3D-FLGN15 symmetrical half-cell does not short-circuit during a long-time galvanostatic cycle. It is worth noting that the long-time galvanostatic test for the 3D-FLGN15|LLZTO|3D-FLGN15 symmetric half-cell has a much longer cycle time than the symmetric half-cell reported in Figure 2b and Table S3. Since the 3D-FLGN15|LLZTO|3D-FLGN15 symmetric half-cell has an ultra-low interface resistance and a high CCD, a long-time galvanostatic test at 2.5 mAh cm^{-2} ultra-high area specific capacity was attempted. As shown in Figure 2c-f, the 3D-FLGN15|LLZTO|3D-FLGN15 symmetrical half-cell can still cycle steadily for more than 1500 h at a high current density of 0.5 mA cm^{-2} and an ultra-high area capacity of 2.5 mAh cm^{-2}. To our knowledge, the ultra-high area capacity of 2.5 mAh cm^{-2} is the highest reported in the literature for long-time galvanostatic

cycling tests (Figure 2g and Table S4). The excellent long-time galvanostatic cycling performance with ultra-high area-specific capacity indicates that the 3D-FLGN15 greatly improves the Li^+ flux and Li^+ transport kinetics at the interface. Meanwhile, the ultra-long time galvanostatic cycling demonstrates once again that the 3D foam structure can effectively inhibit Li dendrite growth and is a great inspiration for the construction of Li dendrite growth-free interfaces.

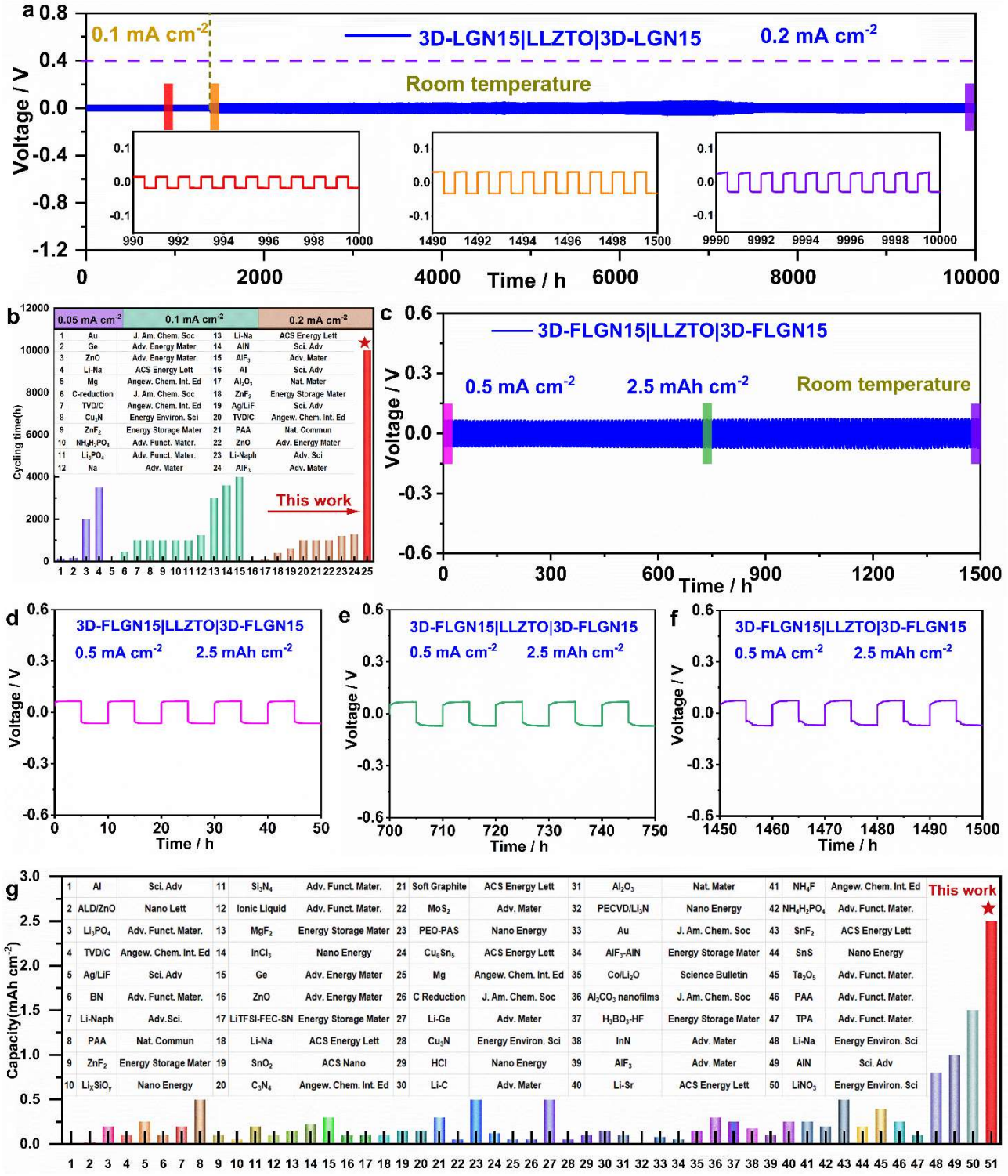

Figure 2. Galvanostatic cycling performance test for Lithium symmetrical half-cells. (a) Galvanostatic cycling performance of the 3D-FLGN15|LLZTO|3D-FLGN15 cell under 0.1~0.2 mA cm^{-2} at RT. (b) Comparison graph of galvanostatic cycle times for Li symmetrical half-cells. The details of the references are shown in Table S3. (c) Galvanostatic cycling performance of the 3D-FLGN15|LLZTO|3D-FLGN15 cell under 2.5 mAh cm^{-2} at RT. (d-f) Enlarged view of the galvanostatic curve

under the current density of 2.5 mAh cm^{-2}. (g) Comparison graph of Li symmetrical half-cell galvanostatic cycling area capacity. The details of the references are shown in Table S4.

From the above analysis, it can be shown that the 3D-FLGN15 composite anode greatly reduces the Li|LLZTO interfacial resistance and inhibits the growth of Li dendrites. Therefore, this lays a solid foundation for the use of high-specific energy LRMO cathode in garnet-based SSB. However, the rapid capacity and voltage decay and very poor rate performance present in LRMO cathodes are difficult to overcome. [47] Encouragingly, the LRMO|LLZTO|3D-FLGN15 full cell has an ultra-high discharge specific capacity of 245 mAh g^{-1} at 0.1C (Figure S17). More importantly, it has a discharge specific capacity of 170 mAh g^{-1} at 1C (1C = 250 mAh g^{-1}), which is much higher than that of the LRMO-based SSB at 1C reported in the literature so far [18-19] (Figure 3f), and is also comparable to that of the pure LE cell (Figure S18), showing a very good rate performance (**Figure 3**a-b). It is interesting to note that after the rate test, the LRMO|LLZTO|3D-FLGN15 full cell can achieve a capacity recovery rate of 99.6% (Figure 3a), which is much higher than the pure LE cell (95.9% capacity recovery rate, Figure S18). The high capacity recovery rate is due to less interfacial side reactions, and the high Li^+ flux and outstanding inhibition of Li dendrite growth of the 3D foamed composite anode (3D-FLGN15) provide a solid basis for the exceptional rate performance of the LRMO|LLZTO|3D-FLGN15 full cell. At the same time, the cycling performance of the LRMO|LLZTO|3D-FLGN15 full cell is further evaluated. As shown in Figure 3c-d, the LRMO|LLZTO|3D-FLGN15 full cell was cycled 200 cycles at 0.2C without capacity decay (~100%) demonstrating excellent cycling performance, which is much higher than that of other Li-rich oxide cathode-based SSB reported in the literature (Figure 3e). [18-20] In addition, it should be noted that the capacity retention of LRMO in LE-based cells was seriously decreased to 65.4% after 150 cycles (Figure S19). Voltage decay is one of the most critical issues for Li-rich cathode in LE-based batteries, which is largely associated with irreversible OAR and structure degradation. [48] It is also quite important to know the voltage behavior of Li-rich cathode in SSBs. But the voltage behaviors have not been evaluated and reported in the previous few LRMO-based SSBs. [18-20] Impressively, the LRMO|LLZTO|3D-FLGN15 full cell showed a 96.21% voltage retention after 200 cycles at 0.2C and an average voltage decay of just 0.66 mV/cycle (Figure 3d), demonstrating a largely mitigated voltage decay. In contrast, the voltage decay of LRMO in LE-based cells was about 2.96 mV/cycle (Figure S20). The extremely low voltage decay in LRMO|LLZTO|3D-FLGN15 even shows great advantages when compared to other LE-based cells with modified LRMO cathodes reported in the extensive literature (Figure 3g and Table S5). In addition, LRMO|LLZTO|Li full cells with pure Li as the anode, due t o their large interfacial impedance at the Li|LLZTO interface, still short-circuit on the first cycle, even at very low currents (Figure S21). In addition, the LRMO|LLZTO|LE|Li full cell was similarly short-circuited after 3 cycles at 0.2C by lowering the Li|LLZTO interface between pure Li and LLZTO by dripping LE (Figure S22). As a further assessment of the cycling performance of the LRMO|LLZTO|3D-FLGN15 full cell, it can be cycled steadily for more than 200 cycles at 0.5C and still maintain a high capacity retention rate (up to 85.1%, Figure S23). Furthermore, under the same conditions, the capacity retention of a pure LE full cell is only 67.3% (Figure S24). It is clear from the above experiments that the excellent interfacial properties of 3D-FLGN15 composite anode can greatly improve the performance of LRMO-based full cells and is one of the best choices of anode materials for high-specific energy SSBs.

LRMO|LLZTO|3D-FLGN15 full cells show excellent cycling performance and very low voltage decay. To explore the differences between LRMO|LE|Li and LRMO|LLZTO|3D-FLGN15 full cells, we performed XPS analyses of the LRMO cathode undercharging to 4.8V(C-4.8V) and discharging to 2.0V(D-2.0V) states, respectively. As shown in **Figure 4**a and 4e, when charged to 4.8V, very weak peaks are detected on the LRMO surface of the LRMO|LE|Li full cell at 529.5 eV (marked as cyan) and 530.5 eV (marked as red), which are attributed to lattice oxygen (O^{2-}) and a lower electron density oxygen species (O_2^{n-}), respectively. [49] In contrast, very strong oxygenated deposit species and LE decomposition were calibrated at 531.7 eV (marked as dark yellow) and 533 eV (marked as green). [50,51] This is due to the decomposition of a large amount of LE as a result of irreversible oxygen release during the cycling process and severe interfacial side reactions, resulting in the formation of large oxygenated deposit species at the interface. [51] When discharged to 2.0V (Figure 4b and 4f), the peaks of O^{2-} and O_2^{n-} were not detected because the LRMO cathode of the LRMO|LE|Li full cell was covered by a large amount of LE decomposition products and oxides, and after etching for 20 nm, a weak O_2^{n-} peak appeared at this time, implying that a large amount of decomposition of the LE had occurred during the first cycling process, and the same result could be observed at the Mn 2p peak, even though the same result can also be observed in the Mn 2p peak, even after etching 20nm, the Mn 2p peak is still undetectable (Figure 4i and 4j). It is worth noting that the decomposition of the LE is widely recognized as one of the main causes of poor cycling performance, rapid voltage decay and undesirable rate performance. [52] Compared to the LRMO|LE|Li full cell, the LRMO|LLZTO|3D-FLGN15 full cell shows very weak peaks of decomposition products at both C-4.8V (Figure 4c and 4g) and D-2.0V (Figure 4d and 4h) and greatly improves the retention of O^{2-} and O_2^{n-} in the surface region, indicating that the SSB can inhibit the side reactions at the interface improving the reversibility of the oxygen redox reaction. In addition, the intensity of the Mn 2p peak before and after etching is not much different (Figure 4k and 4l), indicating that the LRMO cathode in the LRMO|LLZTO|3D-FLGN15 full cell is not covered by the reaction products, which further suggests that the interfacial side reaction during the battery cycling can be effectively reduced in the SSB condition. On the anode side, $LiPF_6$ peaks can be detected on the Li metal of the LRMO|LE|Li full cell, which is due to the $LiPF_6$ residue in the LE. In addition, a large number of LE decomposition products, $Li_xPO_yF_z$ and LiF, can be observed at C-4.8V (Figure S25a and b), [52] while a further $LiPF_6$ decomposition product, PF_5, can be

observed at D-2.0V (Figure S25c and d), [53] further suggesting that a large amount of LE decomposition occurs under the first cycle. Since a trace amount of LE (just 7 μL) was added to the Li|LE|LRMO full cell for wetting the LLZTO|LRMO interface, small amounts of $Li_xPO_yF_z$ and LiF were observed on the LLZTO surface in addition to residual $LiFP_6$. Notably, LaF_3 peaks were also observed on the LLZTO surface due to the formation of LaF_3 and Li from the reaction of LLZTO with HF in LE. [54] Unlike the Li|LE|LRMO full cell, $LiFP_6$ and LiF dominate on the surface of LLZTO, and the decomposition product of $LiFP_6$, PF_5, does not appear, while the peaks of LaF_3 newly appear (Figure S26a and c). $LiFP_6$ comes from the residue of the electrolyte after drying, and LiF comes from two aspects, on the one hand, it is the decomposition of LE. Since the XPS does not show PF_5 and the $Li_xPO_yF_z$ content is very low, it means that only a very small part of the LE is decomposed. On the other hand, it comes from the reaction between LLZTO and HF in LE to form LiF and LaF_3, and the content of LaF_3 gets higher and higher as the etching reaches 20 nm (Figure S26b and d), so we believe that LiF mainly comes from the latter, which also proves that the decomposition of LE in the SSB is very little. In addition, since the 3D-FLGN15 composite anode and LE are separated by LLZTO, the decomposition of LE into products is completely undetectable in 3D-FLGN15 (Figure S26e), which completely avoids the corrosion of LE on the anode, which guarantees the superior performance of the LRMO|LLZTO|3D-FLGN15 full cell.

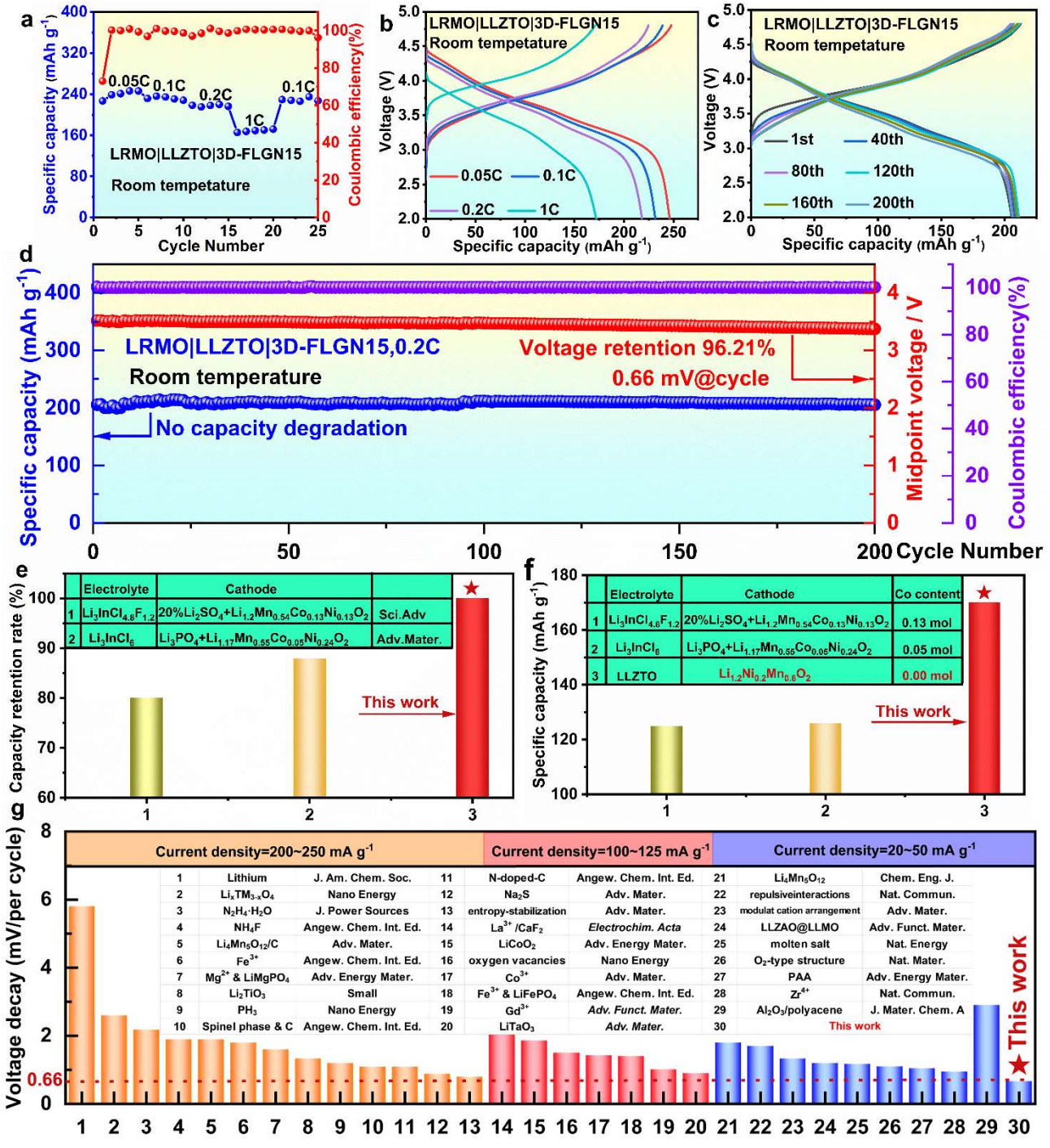

Figure 3. LRMO|LLZTO|3D-FLGN15 full cell performance test. (a-b) Rate performance of the LRMO|LLZTO|3D-FLGN15 full cell. (c) Cycle performance of the LRMO|LLZTO|3D-FLGN15 full cell under 0.2C at RT. (d) Voltage decay and cycle of the LRMO|LLZTO|3D-FLGN15 full cell under 0.2C at RM. (e) Comparative capacity retention rate of SSB after cycling at 0.2C. [18,19] (f) Comparison chart of the discharge-specific capacity of solid-state batteries at 1C. [18,19] (g) Comparison of voltage decay with Liquid Battery. The details of the references are shown in Table S5.

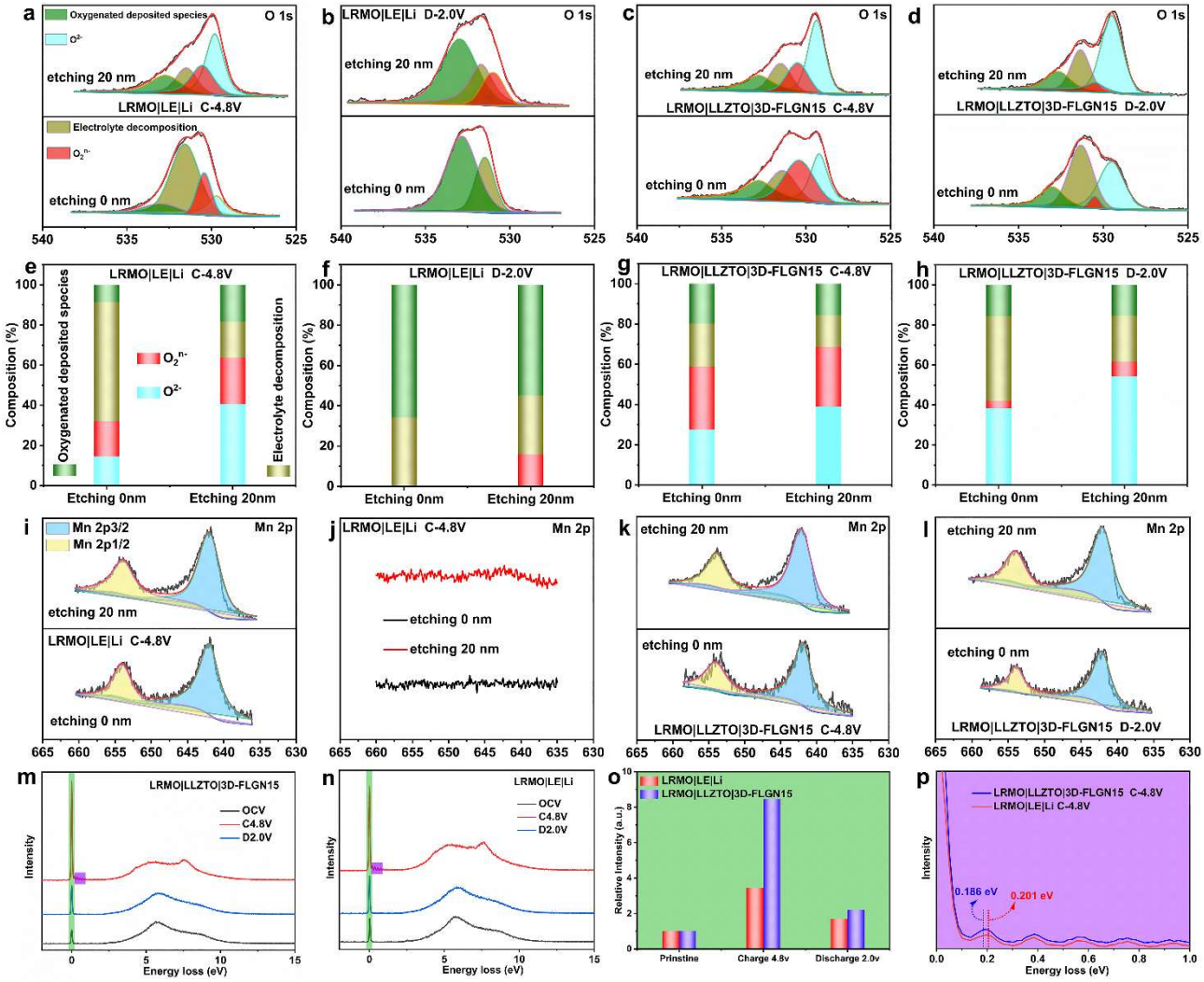

Figure 4. (a-b) O 1s XPS of LRMO cathode of LRMO|LE|Li full cell at 4.8V and 2.0V, respectively. (c-d) O 1s XPS of LRMO cathode of LRMO|LLZTO|3D-FLGN15 full cell at 4.8V and 2.0V, respectively. (e-f) The content of different oxidized species at the LRMO cathode in LRMO|LE|Li full cell at C-4.8 V and D-2.0 V, respectively. (g-h) The content of different oxidized species at the LRMO cathode in LRMO|LLZTO|3D-FLGN15 full cell at C-4.8 V and D-2.0 V, respectively. (i-j) Mn 2p XPS of LRMO cathode of LRMO|LE|Li full cell at 4.8V and 2.0V, respectively. (k-i) Mn 2p XPS of LRMO cathode of LRMO|LLZTO|3D-FLGN15 full cell at 4.8V and 2.0V, respectively. (m) The normalized O–K-edge RIXS of LRMO cathode in LRMO|LLZTO|3D-FLGN15 full cell in different states. (n) The normalized O–K-edge RIXS of LRMO cathode in LRMO|LE|Li full cell in different states. (o) The corresponding RIXS process and the relative elastic peak area of the two LRMO cathode, setting the elastic peak area of each sample in the pristine state as 1. (p) Enlarged image in (m) and (n) at energy loss from 0 to 1.0 eV for the O–O vibration.

OAR is one typical characteristic in Li-rich oxide cathodes which has been extensively explored in LE-based cells. [55-57] Knowing about the OAR behavior of LRMO in SSBs is also quite important. RIXS has a very good sensitivity to the oxidation state of O, [58] and for this reason, it is applied to detect the state of O^{2-} at different voltages on the LRMO cathode both in SSBs and LE-based cells. As shown in Figure 4m and 4n, the reflected loss-energy signals near 5.75 eV come from the TM-O hybridization and O^{2-}2P characteristic peaks. [59] At charging to 4.8 V, a new characteristic peak appears near 7.7 eV, which is attributed to the characteristic peak of O^{2-} redox. [58] It can also be observed that the intensity of the elastic peak gradually increases with charging up to 4.8V, implying that the oxygen vacancies produced by oxygen ions during the redox process gradually increase. [60] The elastic peak intensities of the LRMO cathode at different voltages were compared with the elastic peak intensities of the pristine samples and can be seen from Figure 4o that the elastic peak intensities of the LRMO cathode in the LRMO|LLZTO|3D-FLGN15

full cell were much higher than the pristine samples at a voltage of 4.8V, which indicates that the anions in the LRMO cathode have a higher redox activity in the SSB. When the discharge was completed (2.0v), the elastic peak at the LRMO had the same with higher intensity in SSB, implying that the O^{2-} in LRMO has better redox reversibility in SSB. In addition, the vibration of 0.1-1.0 eV near the elastic peak can reflect the potential fine structure of the LRMO cathode, and its vibration frequency is strongly correlated with the species of O-O dimer. [61] For the LRMO cathode in Li|LE|LRMO full cell, the energy loss peak at ~0.201 eV originates from an O-O vibration with a frequency of 1600 cm^{-1} and is closely related to the molecular O, suggesting localized O_2 molecular and Mn-O bond breakage. [47] In the LRMO|LLZTO|3D-FLGN15 full cell, the loss energy of the LRMO cathode is only 0.186 eV, which at this time is consistent with the 1500 cm^{-1} frequency (Figure 4p), implying that the O-O dimer has a stronger interaction with Mn at the lattice, suggesting that the redox-active O-Mn bond is more robust.[47] Meanwhile, the first-circle in situ XRD also shows that the diffraction peaks of LRMO|LLZTO|3D-FLGN15 have less variation compared with Li|LE|LRMO, which proves that the LRMO cathode has better structural stability during the charging/discharging process of LRMO|LLZTO|3D-FLGN15 (Figure S27).

Conclusion

In summary, we successfully built an LRMO-based SSB using LLZTO as the SE and 3D-FLGN15 composite as the anode. The 3D-FLGN15 composite has a very good wettability (its CA is only 18°) and outstanding interfacial property for LLZTO. The 3D-FLGN15|LLZTO|3D-FLGN15 symmetric half-cells have a high CCD and impressive ASR (1.4 mA cm^{-2} and 1.53 Ω cm^2, respectively), and they can be stably cycled for 10,000h at 0.1-0.2 mA cm^{-2} current density, and can still be steadily cycled for 1,500h even at a high current density of 0.5 mA cm^{-2} and an ultra-high area capacity of 2.5 mAh cm^{-2}, showing excellent interfacial stability. In addition, the 3D-FLGN15|LLZTO|3D-FLGN15 full cell has a 245 mAh g^{-1} discharge specific capacity and a voltage decay of only 0.66 mV/ cycle with great cycling performance (200 cycles at 0.2C without capacity degradation). Moreover, it is found that the OAR reversibility of LRMO in SSB is greatly enhanced in compared to liquid electrolyte-based cells. This work provides a distinct solution to the interface issue of garnet-based SE and is also worthy of consideration for the optimization of other types of SE. More importantly, it shows great potential for the development and application of LRMO-based SSBs.

Acknowledgements

This work was supported by the National Natural Science Foundation of China (Grant No.22005302, 12275362 and 11975238), the International Partnership Program (Grant No. 211211KYSB20170060 and 211211KYSB20180020), the Scientific Instrument Developing Project (Grant No. ZDKYYQ20170001), the Strategic Priority Research Program (Grant No. XDB28000000) of the Chinese Academy of Sciences, and the Natural Science Foundation of Beijing (Grant No. 2182082). This work was also supported by the Fundamental Research Funds for the Central Universities, the China Postdoctoral Science Foundation (2020M680648).

Keywords: Lithium-rich oxide cathode, Solid-state battery, Garnet-based solid electrolytes, Interfacial modification, Suppression of Li dendrites.

References:

[1] JB. Goodenough, K-S. Park, *J. Am. Chem. Soc.* **2013**,135, 1167.
[2] J. M. Tarascon, M. Armand, *Nature,* **2001**,414, 359.
[3] M. Armand, J. M. Tarascon, *Nature,* **2008**,451, 652.
[4] Z. Zhu, D. Yu, Y. Yang, C. Su, Y. Huang, Y. Dong, I. Waluyo, B. Wang, A. Hunt, X. Yao, J. Lee, W. Xue, J. Li, *Nat. Energy,* **2019**,4, 1049.
[5] Liu, Y. Wu, X. Wang, K. Feng, Z. Cheng, T. Liu, Y. Wang, M. Chen, R. Xu, L. Zhou, J. Lu, Y. Guo, B. *Adv. Energy Mater,* **2021**,4,2000982-2000992.
[6] A. Manthiram, *ACS Cent. Sci* **2017**,3, 1063–1069.
[7] S. Jiao, J. Wang, Y-S.Hu, X. Yu, H. Li, *ACS Energy Lett* **2023**, 8, 3025–3037.
[8] Q. Li, D. Ning, D. Wong, K. An, Y. Tang, D. Zhou, G. Schuck, Z. Chen, N. Zhang, X. Liu, *Nat Commun* **2022**,13, 1123.
[9] J.Huang, B. Ouyang, Y. Zhang, L. Yin, D-H. Kwon, Z. Cai, Z. Lun, G. Zeng, M.vBalasubramanian, G. Ceder, *Nat. Mater* **2023**,22, 353.
[10] W .He, W. Guo, H. Wu, L. Lin, Q. Liu, X. Han, Q. Xie, P. Liu, H. Zheng, L. Wang, X. Yu, D-L. Peng, *Adv.Mater* **2021**,33,2005937.
[11] Y. Wang, Z. Li, Y. Hou, Z. Hao, Q. Zhang, Y. Ni, Y. Lu, Z. Yan, K. Zhang, Q. Zhao, F. Li, J. Chen, *Chem. Soc. Rev* **2023**,52, 2713.
[12] Z. Zeng, V. Murugesan, K. Han, X. Jiang, Y. Cao, L. Xiao, X. Ai, X. Yang, J-G. Zhang, M. Sushko, J. Liu, *Nature Energy* **2018**,3, 674.
[13] C. Zhan, T-P. Wu, J. Lu, K. Amine, *Energy Environ. Sci.* **2018**,11, 243.
[14] J. Zhao, X. Zhang, Y. Liang, Z. Han, S. Liu, W. Chu, H. Yu, *ACS Energy Lett.* **2021**,6, 2552.
[15] J.Betz, J. Brinkmann, R. Nolle, C. Lurenbaum, M. Kolek, M. Stan, M. Winter, T. Placke, *Adv.Energy Mater.* **2019**,9,1900574.
[16] C.Zhan, J. Lu, A. Kropf, T. Wu, A. Jansen, Y-K. Sun, X. Qiu, K. Amine, *Nat Commun* **2013**,4, 2437.
[17] W. Liu, J. Li, W. Li, H. Xu, C. Zhang, X. Qiu, *Nat Commun* **2020**,11, 3629.
[18] R .Yu, C.Wang, H. Duan, M. Jiang, A. Zhang, A. Fraser, J. Zuo, Y. Wu, Y. Sun, Y. Zhao, J. Liang, J. Fu, S. Deng, Z. Ren, G. Li, H. Huang, R. Li, N. Chen, J. Wang, X. Li, C. Singh, X. Sun, *Adv. Mater.* **2023**,35, 2207234.
[19] S.Sun, C-Z. Zhao, H. Yuan, Z-H. Fu, X. Chen, Y. Lu, Y-F. Li, J-K. Hu, J. Dong, J-Q.Huang, M. Ouyang, Q. Zhang, *Sci. Adv* **2022**,8, eadd5189.
[20] W. Du, Q. Shao, Y. Wei, C. Yan, P. Gao, Y. Lin, Y. Jiang, Y. Liu, X. Yu, M. Gao, W. Sun, H. Pan, *ACS Energy Lett.* **2022**, 7, 3006.
[21] S. Song, B. Chen, Y. Ruan, J. Sun, L. Yu, Y. Wang, J. Thokchom, *Electrochimica Acta* **2018**,270,501.
[22] G.Lu, Z. Dong, W. Liu, X. Jiang, Z. Yang, Q. Liu, X. Yang, D. Wu, Z. Li, Q. Zhao, X. Hu, C. Xu, F. Pan, *Science Bulletin* **2021**,66,1746.
[23] B.Chen, J. Zhang, T. Zhang, R. Wang, J. Zheng, C. Liu, X. Liu, *ACS Energy Lett.* **2023**,8, 2221.
[24] J-P. Contour, A. Salesse, M. Froment, M. Garreau, J. Thevenin, D-J. Warin, **1979**, 4, 483.
[25] M.Du, Y. Sun, B. Liu, B. Chen, K. Liao, R. Ran, R. Cai, W. Zhou, Z. Shao, *Adv. Funct. Mater.* **2021**,31, 2101556.
[26] J.Wen, Y. Huang, J. Duan, Y. Wu, W. Luo, L. Zhou, C. Hu, L. Huang, X. Zheng, X.Yang, Z.Wen, Y. Huang, *ACS nano* **2019**,13, 14549.

[27] Z. Wang, S. Xie, X. Gao. X. Chen, L. Cong, J. Liu, H. Xie, C. Yu, Y. Liu, *Chinese Chemical Letters* **2023**,15,108151.

[28] Elaboration. Denis A, Université Sciences et Technologies-Bordeaux I, 2003.

[29] M. Hong, Q. Dong, H. Xie, B-C. Clifford, J. Qian, X. Wang, J. Luo, l. Hu, *ACS Energy Lett* **2021**,6, 3753.

[30] M-U. Khan, C-M. Furqan, J. Kim, S-A. Khan, Q-M. Saqid, M-Y. Chougale, R-A.Shaukat, M-H. Kang, N-P. Kobayashi, J. Bea, H-S. Kuok, *ACS Appl. Electron. Mater* **2022**,4, 1, 297.

[31] J. Meng, Y. Zhang, X. Zhou, M. Lei, C. Li, *Nat Commun* **2020**,11, 3716.

[32] Y. Ould-Metidji, L. Bideux, D. Baca, B. Gruzza, V. Matolin, *Applied Surface Science* **2003**,212, 614.

[33] P-C.Wu, T-H. Kim, A. Suvorova, M. Giangregorio, M. Saunders, G. Bruno, A-S. Brown, M. Losurdo, *small* **2011**,7, 751.

[34] H. Xu, Y. Li, A. Zhou, N. Wu, S. Xin, Z. Li, J-B. Goodenough, *Nano Lett.* **2018**,18, 7414.

[35] G. Lu, M. Li, P. Chen, W. Zheng, Z. Yang, R. Wang, C. Xu, *Energy Environ. Sci* **2023**,16, 1049.

[36] A-M. Hafez, Y. Jiao, J. Shi, Y. Ma, D. Cao, Y. Liu, H. Zhu, *Adv. Mater* **2018**,30, 1802156.

[37] Y. Ruan, Y. Lu, Y. Li, C. Zhang, J. Su, J. Jin, T. Xiu, Z. Song, M. Badding, Z. Wen, *Adv. Funct. Mater.* **2021**,31, 2007815.

[38] Z. Bi, Q. Sun, M. Jia, M. Zuo, N. Zhao, X. Guo, *Adv. Funct. Mater.* **2022**, n/a 2208751.

[39] G.Lu, W. Liu, Z. Yang, Y. Wang, W. Zhang, R. Deng, R. Wang, L. Lu, C. Xu, *Adv. Funct. Mater.* **2023**,n/a, 2304407.

[40] J.Xie, J. Wang, H. Lee, K. Yan, Y. Li, F. Shi, W. Huang, A. Pei, G. Chen, R.Subbaraman, J. Christensen, Y. Cui, *Sci. Adv.* **2018**,4, eaat5168.

[41] Z.Wang, X. Li, Y. Chen, K. Pei, Y. Mai, S. Zhang, J. Li, *Chem* **2020**,6, 2878.

[42] Y. Lu, C-Z. Zhao, J-Q. Huang, Q. Zhang, *Joule* **2022**,6,1172.

[43] J. Wei, B. Luo, Q. Wang, C. Yu, Z. Liu, Z. Zao, R. Zhao, S. Wang, X. Wang, B. Zhang, J. Zhang, J. Hou, J. Liang, *Adv. Energy Mater.* **2023,** n/a, 2300165.

[44] M.Muller, J. Schmieg, S. Dierickx, J. Joos, A. Weber, D. Gerthsen, E. Ivers-Tiffee, *ACS Appl. Mater. Interfaces* **2022**,14, 14739.

[45] Y. Chien, H. Liu, A. Menon, W. Brant, D. Brandell, M. Lacey, *Nat Commun* **2023**,14, 2289.

[46] Q. Zhao, X. Liu, S. Stalin, K. Khan, L-A. Archer, *Nat. Energy* **2019**,4, 365.

[47] J. Zhang, Q. Zhang, D. Wong, N. Zhang, G. Ren, L. Gu, C. Schulz, L. He, Y. Yu, X. Liu, *Nat Commun* **2021**,12, 3071.

[48] T. Liu, J. Liu, L. Li, L, Yu, J. Diao, T. Zhou, S. Li, A. Dai, W. Zhao, S. Xu, Y. Ren, L. Wang, T. Wu, R. Qi, Y. Xiao, J. Zheng, W. Cha, R. Harder, *Nature* **2022**,606, 305.

[49] C. Shen, Y. Liu, L. Hu, W. Li, X. Liu, Y. Shi, Y. Jiang, B. Zhao, J. Zhang, *Nano Energy* **2022**,101, 107555.

[50] Z. Sun, X. Wang, H. Zhao, S-W. Koh, J. Ge, Y. Zhao, P. Gao, G. Wang, H. Li, *Carbon Energy* **2020**,2, 122.

[51] M.Sathiya, G. Rousse, K. Ramesha, C-P. Laisa, H. Vezin, M-T. Sougrati, M.L. Doublet, D. Foix, D. Gonbeau, D. W. Walker, *Nat. Mater.* **2013**,12, 827.

[52] W. Liu, J. Li, W. Li, H. Xu, C. Zhang, X. Qiu, *Nature Communications* **2020**,11,3629.

[53] W. Yu, Z. Yu, Y. Cui, Z. Bao, *ACS Energy Lett.* **2022**,7, 3270.

[54] B. Chen, J. Zhang, T. Zhang, R. Wang, J. Zheng, Y. Zhai, X. Liu, *Adv. Sci.* **2023**,10, 2207056.

[55] S. Kang, D. Choi, H. Lee, B. Choi, Y-K. Kang, *Adv. Mater.* **2023**,n/a, 2211965.

[56] Y. Yang, C. Gao, T. Luo, J. Song, T. Yang, H. Wang, K. Zhang, Y. Zuo, W. Xiao, Z.Jiang, T.Chen, D. Xia, *Adv. Mater.* **2023**, n/a, 2307138.

[57] E.McCalla, A-M. Abakumov, M. Saubanere, D. Foix, E-J. Berg, G. Rousse, M-L.Doublet, D. Gonbeau, P. Novak, *Science* **2015**,350, 1516.

[58] Q. Li, D. Ning, D. Zhou, K. An, D. Wong, L. Zhang, Z. Chen, G. Schuck, C. Schulz, Z. Xu, G. Schumacher, X. Liu, *J. Mater. Chem. A* **2020**,8,7733.

[59] J.Xu, M. Su, R. Qiao, W. Renfrew, L. Ma, T. Wu, S. Hwang, D. Nordlund, D. Su, K.Amine, j. Lu, B. McCloskey, W. Yang, W. Tong, *Nat Commun* **2018**,9, 947.

[60] K.Luo, M-R. Roberts, R. Hao, N. Guerrini, D-M. Pickup, Y-S. Liu, K. Edstrom, J.Guo, A-V. Chadwick, L-C.Duda, P-G. Bruce, *Nat. Chem* **2016**,8, 684.

[61] R.House, U. Maitra, M. Perez-Osorio, J. Lozano, L. Jin, J. Somerville, L. Duda, A.Nag, A. Walters, K. Zhou, M. Roberts, P. Bruce, *Nature* **2020**,577, 502.

Table of Contents

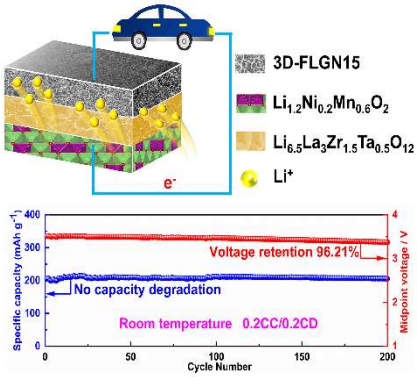

We successfully constructed a high-performance solid-state battery based on Li-rich $Li_{1.2}Ni_{0.2}Mn_{0.6}O_2$ cathode, $Li_{6.5}La_3Zr_{1.5}Ta_{0.5}O_{12}$ solid electrolyte and GaN-modified Li anode. The assembled Li symmetric cell shows quite low interfacial resistance and great interfacial stability, and the full battery shows a high initial capacity, a high capacity retention, a high rate capability and a significantly mitigated voltage decay demonstrating a great potential in high energy density solid-state battery.

Li-rich $Li_{1.2}Ni_{0.2}Mn_{0.6}O_2$ cathode, $Li_{6.5}La_3Zr_{1.5}Ta_{0.5}O_{12}$ solid electrolyte and GaN-modified Li anode assembly of solid-state batteries with excellent performance. Li symmetric cell have very low interfacial resistance and great interfacial stability. The full cell has the advantages of high initial capacity, high rate, high-capacity retention and low voltage decay.